JOURNAL OF GEOPHYSICAL RESEARCH, VOL. 96, NO. C8, PAGES 15,093–15,103, AUGUST 15, 1991

Ocean Data Assimilation Using Optimal Interpolation With a Quasi-Geostrophic Model

MICHELE M. RIENECKER

Oceans and Ice Branch, NASA Goddard Space Flight Center, Greenbelt, Maryland

ROBERT N. MILLER

College of Oceanography, Oregon State University, Corvallis

Optimal interpolation (OI) has been used to produce analyses of quasi-geostrophic (QG) stream function over a 59-day period in a 150-km-square domain off northern California. Hydrographic observations acquired over five surveys, each of about 6 days' duration, were assimilated into a QG open boundary ocean model. Since the true forecast error covariance function required for the OI is unknown, assimilation experiments were conducted separately for individual surveys to investigate the sensitivity of the OI analyses to parameters defining the decorrelation scale of an assumed error covariance function. The analyses were intercompared through dynamical hindcasts between surveys, since there were too few independent data for other verification of the various analyses. For the hindcasts, the QG model was initialized with an analysis for one survey and then integrated according to boundary data supplied by the corresponding analysis for the next survey. Two sets of such hindcasts were conducted, since there were only three statistically independent realizations of the stream function field for the entire observing period. For the irregular sampling strategy of the first half of the observing period, the best hindcast was obtained using the smooth analyses produced with assumed error decorrelation scales identical to those of the observed stream function (about 80 km): the root mean square difference between the hindcast stream function and the final analysis was only 23% of the observation standard deviation. The best hindcast (with a 31% error) for the second half of the observing period was obtained using an initial analysis based on an 80-km decorrelation scale and a final analysis based on a 40-km decorrelation scale. The change in decorrelation scale was apparently associated with a change in sampling strategy and the importance of the resolution of small-scale vorticity input across the open boundary. The last survey used a regular sampling scheme with good coverage (about 20-km resolution) of the entire domain so that smaller-scale features were resolved by the data. The earlier surveys used a coarser (about 75 km) sampling resolution, and smaller-scale features that were not well-resolved could not be inferred correctly even with short error covariance scales. During the hindcast integrations, the dynamical model effectively filtered the stream function fields to reduce differences between the various initial fields. Differences between the analyses near inflow boundary points ultimately dominated the differences between dynamical hindcasts. Analyses for the entire 59-day observing period of the five independent surveys were produced using continuous assimilation. A modified form of OI in which the forecast error variances were updated according to the analysis error variances and an assumed model error growth rate was also used, allowing the OI to retain information about prior assimilation. The analyses using the updated variances were spatially smoother and often in better agreement with the observations than the OI analyses using constant variances. The two sets of OI analyses were temporally smoother than the fields from statistical objective analysis (OA) and in good agreement with the only independent data available for comparison. Unfortunately, the limiting factor in the validation of the assimilation methodology remains the paucity of observations.

1. INTRODUCTION

Given the sparsity and asynopticity of conventional ocean data, accurate estimates of oceanic fields might best be obtained from a blend of (incomplete, noisy) observations with (imperfect) model output. This paper presents the incorporation of optimal interpolation (OI), the data assimilation technique most commonly used in operational numerical weather prediction (see, for example, *Bengtsson et al.* [1981]) into a quasi-geostrophic (QG) open ocean model to produce synoptic estimates of the QG stream function field off northern California during the summer of 1984.

Various four-dimensional data assimilation techniques similar to those in use or under development in the numerical weather prediction community have been used to estimate initial and boundary conditions and/or forcing for ocean models [e.g., *Bennett and McIntosh*, 1982; *Thacker*, 1988; *Harlan and O'Brien*, 1986] and to forecast or hindcast ocean fields [e.g., *Robinson et al.*, 1986; *Rienecker et al.*, 1987, hereinafter RMR]. Sophisticated techniques such as the Kalman filter or smoother [e.g., *Miller*, 1986; *Miller and Cane*, 1989; *Bennett and Budgell*, 1989; *Gaspar and Wunsch*, 1989] or variational methods [e.g., *Thacker*, 1988; *Long and Thacker*, 1989; *Bennett*, 1990] impose considerable demands on computer resources and are optimal only in the case of linear dynamics. The Kalman filter also requires detailed estimates of the statistics of errors in the forcing and errors due to neglected physics or numerical truncation.

The mechanism for assimilation of data in OI is identical to that in the Kalman filter, except that there is no (time-consuming) prognostic calculation of the model forecast error covariance matrix. Since the true model forecast error

Paper number 91JC01530.
0148-0227/91/91JC-01530$05.00

covariance is unknown, the Kalman filter is necessarily initialized with an error covariance matrix which is arbitrary although, like OI, guided by observations. This initial uncertainty may mean that OI could provide analysis fields, from short-period assimilation into a nonlinear dynamical model integration, with error bounds comparable to those of the Kalman filter but achieved at lower cost.

The availability of data which resolves the ocean mesoscale/synoptic scale is primarily limited to smaller open ocean domains. In its use of eddy resolving data and model for an open ocean domain, the spirit of the present work resembles the work of *De Mey and Menard* [1989] and *De Mey and Robinson* [1987], who used objective analysis (taken here to refer exclusively to statistically optimized interpolation/extrapolation techniques) to supply initial and boundary data to a QG model of an open ocean domain about 6 times the local internal deformation radius. One advantage of OI over the approach of De Mey and Menard or De Mey and Robinson is that periodic reinitialization of the interior field can be used to avoid the instabilities that inevitably develop in long open-boundary integrations [*Miller and Bennett*, 1988].

In contrast, *White et al.* [1990*a*] used OI to assimilate Geosat altimetric observations in the region of the California Current into a closed-basin non-eddy-resolving QG model of the entire North Pacific. Unfortunately, there were no independent observations to assess the accuracy of the assimilation procedure, and in comparison with seasonal structure inferred from long-term observations, no indication was given of how the updated model output (i.e., after assimilation of the surface data) improved upon the model without assimilation. It was clear, however, that the non-eddy-resolving model could not adequately reproduce the multiple core structure of the California Current system (CCS). Although the use of closed basin domains, as in the work of *White et al.* [1990*a*], avoids the difficulties of open boundary conditions, the error covariances at the boundaries between data-dense and data-sparse regions in large domains may require special treatment in the implementation of OI [*Cohn and Morone*, 1984].

The hydrographic data used in this study were acquired in the domain shown in Figure 1 by the Ocean Prediction Through Observations, Modeling, and Analysis (OPTOMA) program during a 59-day experiment comprising five surveys, each of about 6 days' duration [RMR]. Based on an estimated decorrelation time of 20 days, the experiment comprises only three independent surveys. The sensitivity of analyses to the assumed structure of the error covariance function is investigated through independent analyses for separate surveys, produced by assimilating only during the 6 days of the survey. The analyses are assessed through two separate hindcast experiments because of the lack of independent verification data. The error covariance parameters for continuous assimilation over the entire 59-day observing period are chosen on the basis of these hindcast experiments, and a technique is used to update the error variances according to a prescribed model error growth rate in order to produce estimates of the forecast error variance. The model and data assimilation systems are described in section 2. The assimilation experiments themselves are described in section 3, and results are summarized in section 4.

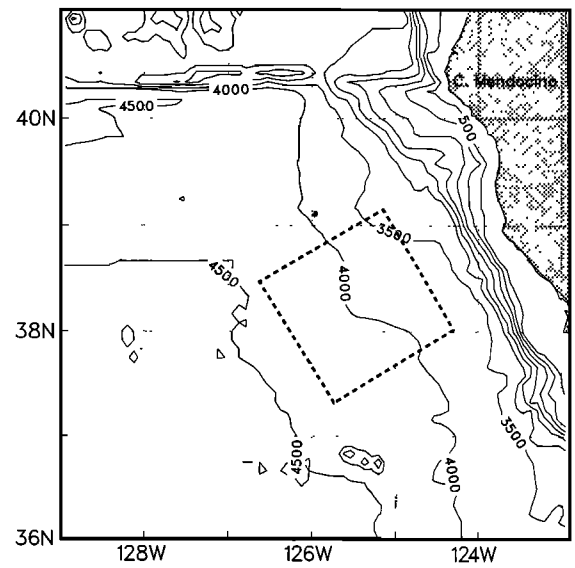

Fig. 1. OPTOMA11 observational domain with bathymetry shown in meters.

2. THE ASSIMILATION SYSTEM

2.1. *Implementation of OI With the QG Model*

The dynamical model used in the assimilation system is the open ocean, QG model described by *Miller et al.* [1983]. The QG potential vorticity ζ evolves according to

$$\frac{D\zeta}{Dt} + \beta\psi_x = F, \tag{1}$$

where ψ is the QG stream function which is determined diagnostically according to

$$\zeta = \nabla^2\psi + \Gamma^2(s\psi_z)_z. \tag{2}$$

In the above, ∇^2 is the horizontal Laplacian operator,

$$\frac{D\zeta}{Dt} = \frac{\partial\zeta}{\partial t} + \alpha J(\psi, \zeta),$$

$$\alpha = t_0\frac{V}{L}, \qquad \beta = t_0\beta_0 L, \qquad \Gamma^2 = \frac{f_0 L^2}{N_0^2 H^2},$$

$$s(z) = \frac{N_0^2}{N^2(z)},$$

J is the Jacobian operator, L is a horizontal length scale of the motion, V is a velocity scale, t_0 is a time scale, f_0 is the Coriolis parameter, β_0 is the gradient of the Coriolis parameter, N_0^2 is the stratification scale, $N^2(z)$ is the average (in space and time) stratification, and H is the scale of thermocline depth variations. Dimensional stream function and potential vorticity are ψVL and $\zeta V/L$, respectively. Subgrid-scale dissipation processes are included in the vorticity equation by use of a Shapiro filter F.

The numerical integration requires initial specification of stream function and vorticity throughout the domain and specification of stream function along the boundary and vorticity at inflow points along the boundary at each subsequent time step [*Charney et al.*, 1950]. In addition, the

vertical velocity at the top and bottom boundaries must be specified at each time step, according to the wind stress curl forcing and bottom topography, respectively.

The OI analysis field, ψ_k^a (written as a vector at time t_k), is the linear, least squares best estimate of the stream function field formed from a correction to the dynamical model forecast field ψ_k^f:

$$\psi_k^a = \psi_k^f + \mathbf{e}_k^f,$$

where the correction $\mathbf{e}_k^f$ is derived from the observations at t_k, ψ_k^o, and the model forecast field:

$$\mathbf{e}_k^f = \mathbf{K}_k(\psi_k^o - \mathbf{H}_k\psi_k^f),$$

where

$$\mathbf{K}_k = \mathbf{P}\mathbf{H}_k^T(\mathbf{H}_k\mathbf{P}\mathbf{H}_k^T + \mathbf{R})^{-1}.$$

$\mathbf{H}_k$ defines the observational scheme at time t_k; the superscript T denotes the matrix transpose, $\mathbf{P}$ is the forecast error covariance matrix, and $\mathbf{R}$ is the observational error covariance. The error covariance of the analysis field, $\mathbf{P}_k^a$, is

$$\mathbf{P}_k^a = (\mathbf{I} - \mathbf{K}_k\mathbf{H}_k)\mathbf{P}, \tag{3}$$

where $\mathbf{I}$ is the identity matrix. The forecast error and the observational error are assumed to be uncorrelated. Details are given by *Miller* [1986].

In the Kalman filter formulation, $\mathbf{P}$ evolves from some initial specification according to the governing dynamics. In oceanographic applications, the correct initial $\mathbf{P}$ is unknown but is chosen to have a "realistic" functional form as estimated from data. In OI, $\mathbf{P}$ usually is held constant or allowed to evolve by a simple scheme. An example of such a simplified evolution scheme for $\mathbf{P}$ is presented by *McPherson et al.* [1979], who transformed the estimated analysis error of an atmospheric data assimilative model into an estimated prediction error by augmenting the former according to an approximation of the model's error growth rate. The estimated prediction error, which was bounded by the climatological variance of the parameters, was used as an indication of the frequency and quality of assimilation updates. The assimilation scheme replaces $\mathbf{P}$ by $\mathbf{P}_k^f$ where (following *Cohn* [1982])

$$\mathbf{P}_k^f = (D_k^f)^{1/2}\mathbf{C}(D_k^f)^{1/2}. \tag{4}$$

Here $\mathbf{C}$ is the forecast error correlation matrix, kept constant in time, and the forecast error variances D_k^f (a diagonal matrix formed from the diagonal of $\mathbf{P}_k^f$) are assumed to grow in time according to

$$D_k^f = D_{k-r}^a + D(r), \tag{5}$$

where D_{k-r}^a is formed from the diagonal of $\mathbf{P}_{k-r}^a$ (see (3)) and $D(r)$ is the prescribed forecast error growth over the r time steps since the last assimilation phase. This technique is employed below, for comparison with that using constant error variances, in the assimilation over the entire OPTOMA 11 survey. The key to the difference between the two forms of OI lies in equation (3), which shows that assimilation reduces the forecast error variance at affected model grid points. If data are assimilated at those grid points at some later time, the constant error variance OI takes no advantage of the increased confidence in the forecast stream function, whereas (if the time between assimilation periods is sufficiently short) the time-dependent variance OI places an increased weight on the model stream function. Unlike the Kalman filter formulation, no account is made for the advection of information.

2.2. *Application to OPTOMA11*

The OPTOMA11 experiment was conducted in June to August 1984. Most of the data were acquired by expendable bathythermograph (XBT) casts in a 150-km-square domain centered approximately 180 km offshore Point Arena in a region of gently sloping bathymetry (Figure 1). The observing system placed emphasis on the acquisition of data on the boundaries of 75-km-square submodules (see Figure 7*e*), with data spaced at about 18 km along these boundaries. The QG stream function used in the dynamical model was calculated from density anomaly profiles and was referenced to 750 km. This reference level was determined iteratively as that which gave the best hindcast in the experiment of RMR. The true reference level is unknown because of an unmeasured barotropic flow component. Density profiles were estimated from the XBT temperature profiles using an average salinity-temperature relation from conductivity-temperature-depth (CTD) data acquired during the experiment. The density anomaly was calculated with reference to the mean profile over the entire experiment. Further details, including the use of empirical orthogonal functions (EOFs) to estimate the density anomaly at the deeper model levels from the anomaly to at least 450 m, are given by RMR. A similar technique for extrapolation of surface data to deeper model levels was used by *De Mey and Robinson* [1987]. The relative error introduced at depth is potentially large, but the absolute error is small, and the technique avoids the introduction of spurious energy in high baroclinic modes which may result if the shallow data are simply inserted at shallow levels as was done by *White et al.* [1990*a*, *b*]. Such errors could be troublesome in this eddy-resolving model.

For this region of the California Current, the vertical structure was resolved with six levels (50, 150, 400, 1070, 2150, and 3380 m for an average ocean depth of 4000 m), and the specific parameters defined above were $V = 10$ cm s^{-1}, $L = 50$ km, $t_0 = 1.0 \times 10^6$ s, $f_0 = 0.91 \times 10^{-4}$ s^{-1}, $\beta_0 = 1.8 \times 10^{-11}$ m^{-1} s^{-1}, $N_0 = 0.011$ s^{-1} and $H = 150$ m. The horizontal grid spacing was 9.4 km, over a 150-km-square domain, and the time step was 2 hours.

For the experiments discussed below, $\mathbf{P}$ (or $\mathbf{C}$) was chosen to have an isotropic, homogeneous functional form similar to the observed stream function covariance. This assumes that the dominant contribution to the error in forecast streamfunction comes from inadequate knowledge of the intensity and phase of the "observed" features and from errors introduced by inadequate knowledge of the boundary values required for the open domain (compare with the scales of the E5 analyses discussed below). Since the observations are assimilated at each model level, some assumption must be made regarding the vertical dependence of $\mathbf{P}$. Two functional forms were tried, the first with depth dependence only in the total variance;

$$P(r, z) = \sigma^2(z)(1 - (r/a)^2)e^{-(r/b)^2}, \tag{6}$$

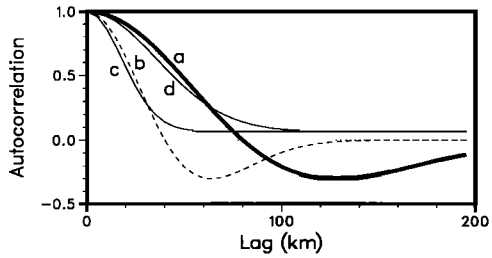

Fig. 2. Covariance functions used for the model error covariance function. Curve a shows function (6) with parameters determined by regression from the observed stream function, (a = 80 km and b = 100 km), used for experiment E1; curve b shows function (6) with (a = 40 km and b = 50 km), used for E2; curve c shows function (7) determined according to modal energies in current meter data with r_0 = 500 km and r_1 = 25 km, used for E3; and curve d shows function (7) with r_0 = 1000 km and r_1 = 50 km, used for E4. Curves c and d are shown for z = 50 m.

with a = 80 km and b = 100 km as determined by regression from the observations, and the second with depth dependence according to the mean barotropic/baroclinic structure [*Rienecker et al.*, 1988] observed in current meter data off the continental slope off northern California,

$$P(r, z) = A\{0.62 \exp[-(r/r_0)^2] + F_1(z) \exp[-(r/r_1)^2]\}, \quad (7)$$

where $F_1(z)$ is the square of the profile of the first baroclinic mode, r is horizontal separation, and z represents the model level in question. For $P(r)$ of (6) to have a physically realizable spectrum, it is sufficient that $2^{1/2}a \geq b$, which is satisfied by the parameter values determined from the observations. For (7), values of r_1 = 25 km and r_0 = 500 km were chosen as representative of the first-mode deformation radius and a larger, external scale, respectively. These choices corresponded to a much shorter decorrelation scale than that estimated from the observations, so r_1 = 50 km and r_0 = 1000 km were also considered. Only one data type was considered (namely, in situ stream function profiles) and data were treated separately at each level; hence A was chosen so the $P(0, 0) = \sigma^2(0)$, the observed stream function variance at the surface. Graphs of (6) and (7) for various parameter choices are shown in Figure 2.

The observational errors were assumed to be uncorrelated, i.e., $R(r) = 0$, if $r \neq 0$. $R(r, z)$ was chosen to be $0.1\sigma^2(z)$, i.e., 10% of the observed stream function variance. This represents the average observation noise variance estimated from closely spaced observations on other OPTOMA surveys by extrapolating the covariance at nonzero lags to zero lag and comparing the result with the calculated variance. The estimate may be justified a posteriori by the point comparison with the observations in the hindcast experiments conducted below.

For the QG model, stream function data were assimilated level by level, with data at one level not directly affecting the analysis field at a different level (the vertical coupling was already accounted for in the EOF treatment of the data and in the assumed error covariance function). Once the analyzed stream function was calculated, the analyzed vorticity was determined from (2) and the fields evolved further according to (1).

3. ANALYSES FROM OPTOMA11

Since the error covariance **P** is unknown, assimilation experiments were conducted to assess the sensitivity of OI analyses to the choice of **P**. In the description below, day 0 corresponds to year day 158 (June 6). Independent analyses were produced for days 6, 21, 36, and 59 of the OPTOMA11 surveys with assimilation starting at days 0, 17, 26, and 56, respectively. These analyses were independent in the sense that none of them was used as an initial estimate for another and they had no data in common. As discussed below, hindcast experiments, conducted as dynamical interpolation between OI analyses, were used to assess the analyses. Based on the estimated 20-day decorrelation time for the fields of these surveys, there were only three statistically independent realizations of the fields over the entire observing period, allowing two independent hindcast experiments. The use of four (rather then three) analyses is dictated by the observing times and the desire to hindcast for about 20 days, the estimated decorrelation time, so that the estimated open boundary data are meaningful.

This study focuses on mesoscale variability, and since the climatological mean flow of the California Current is weak compared with the mesoscale flow (about 4 cm s^{-1} compared to about 50 cm s^{-1} at the surface), the initial field (prior to assimilation) was taken to be $\psi = 0$ for each survey. The analyses were produced by assimilating stream function data once per day, with all data within half a day of the assimilation time treated as simultaneous. Typically, 10 to 20 profiles were assimilated per day. The data distribution per survey is given in Table 1. During the assimilation cycle, the boundary values of stream function and vorticity were kept fixed unless changed by the assimilation process. The results of this sensitivity study were used to choose the form of **P** for the production of analyses of each of the five OPTOMA11 surveys in a continuous assimilation mode. The discussion is restricted primarily to the fields at 50 m, the most energetic level of those used in the model.

3.1. *Sensitivity of the Analyses to Prescribed Covariance Parameters*

To test the sensitivity of the analysis to the prescribed error covariance structure, **P** was modelled in turn as each of the covariance functions (6) and (7). For each of these functions, two sets of parameters were chosen. For (6) these were (a, b) = (80, 100) km (as estimated for the observed stream function itself) and (a, b) = (40, 50) km, denoted below as experiments E1 and E2, respectively. For (7) the parameters were (r_0, r_1) = (500, 25) km (i.e., r_1 specified as the internal deformation radius) and (r_0, r_1) = (1000, 50) km, denoted as experiments E3 and E4, respectively. During

TABLE 1. Assimilated Data Distribution for Each OPTOMA11 Survey

Survey	Observing Dates	Number of Data
1 (AI)	0–6	74
2 (AII)	17–21	79
	22–24	53
3 (DII)	26–30	55
4 (AIII)	32–36	29
5 (DIII)	56–59	68

assimilation, only data within a radius of 75 (40) km of any model grid point were considered for the larger (smaller) decorrelation scales. This restriction of data lessens the influence of inappropriate (i.e., inadequately defined) covariances at large separation on the analysis [*Lorenc*, 1986].

Two other analyses for days 6 and 21 are shown in Figure 3 for comparison: E0 is the statistical objective analysis (i.e., statistically optimized interpolation with no dynamics) produced using (6) when all data in a given survey were assumed simultaneous. E5 represents the stream function determined according to Laplace's equation:

$$\nabla^2\psi = 0,$$

with boundary values provided by the E0 fields. A stream function so determined will have minimum kinetic energy consistent with the boundary values. E5 was performed to identify the extent of boundary control in this small open ocean domain for this realization of the CCS. The experiments are summarized in Table 2 and maps are shown in Figure 3 along with day 21 hindcasts which, as will be described below, are used for comparison purposes.

For day 6, E1 displays a cyclone which penetrates farther into the domain than the other analyses which all have cyclonic features less intrusive than E0. In the northeast quadrant, E1 contains a local high, whereas E2 and E3 contain a local low bounded to the east by small-scale anticyclonic features. In E4 the northeast anticyclone is stronger and of larger scale, and the low to the west has two centers and slightly different orientation compared with E2 or E3. In E0 there is no evidence for either a high or a low in the northwest quadrant (a region with no data in the interior of the quadrant; see Figure 6*e*)–these features in the OI analyses have developed dynamically depending on the corrections made to the model fields during the assimilation phase. The overall shape of the cyclone in E0 is in better agreement with E1 than with the other analyses.

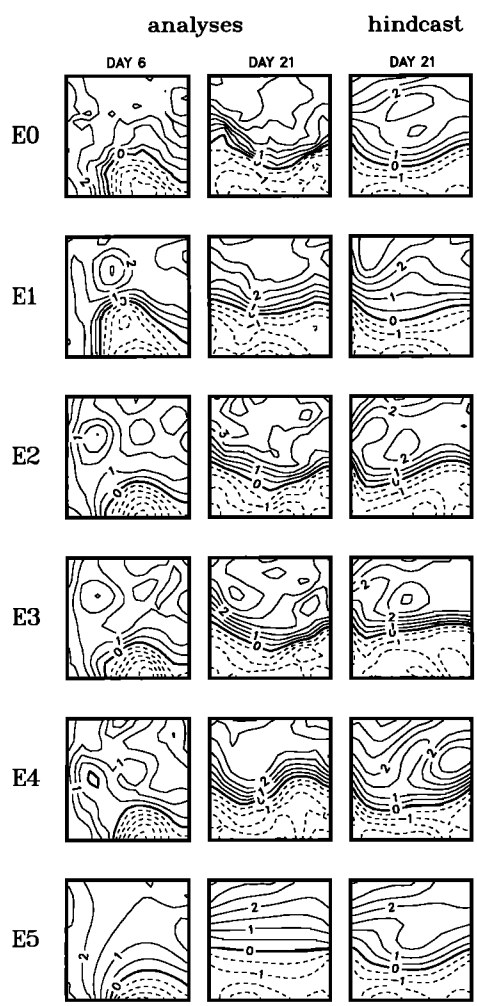

Fig. 3. The analyses of stream function at 50 m (left) for day 6 and (middle) for day 21, and (right) the dynamical hindcast for day 21. The stream function is nondimensional and the contour interval is 0.5. Dashed lines denote negative values; the thick solid line is the zero contour. The experiments are defined in Table 2.

TABLE 2. Definition of Sensitivity Experiments

Experiment	Definition
E0	objective analysis (no dynamics, all observations assumed coincident)
E1	OI using covariance function (6) with a = 80 km, b = 100 km
E2	OI using covariance function (6) with a = 40 km, b = 50 km
E3	OI using covariance function (7) with r_0 = 500 km, r_1 = 25 km
E4	OI using covariance function (7) with r_0 = 1000 km, r_1 = 50 km
E5	interpolation according to Laplace's equation (no statistics, no dynamics)

For day 21 the differences between the analyses lie in the curvature and gradient of the westward flowing jet. In E1 the jet has less curvature and lower gradient than in E2 or E3. In E4 the jet has a more pronounced wavy structure. In E2 and E3 the anticyclone north of the jet has smaller-scale variability than in E1 or E4 because of the shorter covariance scale and radius of influence. At the western boundary, all four OI analyses show a slightly different curvature from that of E0. Otherwise, the curvature in the center of the domain and on the eastern boundary is similar for E0, E2, and E3.

Although the OPTOMA experiment was designed to provide initial, boundary, and verification data for numerical models, its data were still too sparse for a full set of validation experiments to be performed. Such validation experiments would necessarily involve holding back data from the assimilation process. From the number of observations used in the assimilation (see Table 1), it is obvious that there are too few data to do this, since removal of any significant part of the data would degrade the analysis severely and too few points kept back for validation would not provide meaningful statistics.

Since there was no independent "ground truth" field to test the adequacy of the analyses, they were compared through dynamical hindcasts in which the quasi-geostrophic model was initialized with the analysis for day 6 and then integrated forward to day 21. Boundary information was supplied by linear interpolation between the analyses for these two days and the model hindcast the interior field of the later analysis. The comparison of hindcast interior with analysis interior at day 21 for each experiment shows how well the analysis pairs are in quasi-geostrophic balance and are quasi-geostrophically consistent with each other in that one evolves to the other under the assumption of quasi-

TABLE 3. Statistical Assessment of the Dynamical Hindcasts for Day 21

	NRMSD Pointwise Observations	Analyses					
		ψ		$\lvert\nabla\psi\rvert$		ζ	
		C	NRMSD	C	NRMSD	C	NRMSD
E0	0.32	0.95	0.32	0.44	0.72	0.74	0.85
E1	0.35	0.97	0.23	0.44	0.51	0.88	0.55
E2	0.39	0.92	0.38	0.24	0.75	0.65	0.87
E3	0.35	0.93	0.37	0.21	0.89	0.61	0.97
E4	0.35	0.91	0.43	0.25	0.77	0.59	1.02
E5	0.32	0.97	0.28	0.53	0.80	0.77	0.81

For each experiment, comparisons are made between the hindcast and the analysis used to provide the necessary boundary data as well as the observations of the second survey on a pointwise basis. C refers to the correlation; NRMSD is the normalized rms difference. For ψ and ζ the normalization factor is the standard deviation of the observations, 2.03 and 22.7, respectively. For $|\nabla\psi|$ the normalization factor is the mean gradient, 2.3.

geostrophic dynamics. The inadequacy of fit in this case (as represented by the difference measures in Table 3) can be due to errors in the analyses or inadequate lateral and/or vertical boundary information. Although surface forcing by wind stress curl can be important, RMR found that during the initial phase of OPTOMA11 surface forcing had little effect on the hindcast fields and it was not included in these initial integrations. The hindcast was also compared with the individual AII observations on a pointwise basis in space and time. Observational noise and incomplete physics also contribute to inadequacy of fit in this case.

E1 provided the best fit between the dynamically hindcast field and the analysis at day 21 with a normalized root-mean-square stream function difference of only 23% (Table 3). This OI analysis assumed that the model forecast error covariance was the same as that of the ψ field itself. The differences between the hindcast from E5 and the E0 analysis for day 21 were also small, although the difference in lateral and vertical gradients were much larger (by about 30%) than for E1. The difference measures for E0 were only slightly worse. The hindcasts all had comparable agreement with the pointwise observations of AII, with differences consistent with the assumed observational noise variance. The analyses for E3 and E4, which used the depth-dependent covariance function (4), did not produce as good a hindcast as E1, had difference measures comparable to or worse than E2, and had much worse difference measures for potential vorticity.

For a closed model domain, the growth in stream function differences as a function of spatial scale depends on the dominant scales of energy as well as the scale-dependent effect of dissipation [*Adamec*, 1989]. For an open domain, the differences may eventually be advected out of the domain; however, initially, nonlinear instabilities could cause small analysis differences on short scales to grow quickly. This appeared to be the case during the assimilation cycle itself, when intense gradients were sometimes introduced due to the difference of the observations from the initial guess of $\psi = 0$. Differences between E1 and E4 during the assimilation cycle were noticeable within 2 days, primarily because of small differences in the covariance functional form, but also because of lateral and vertical exchange processes. At the deeper model levels, the covariance scales increase for (7) with a concomitant increase in the level of correlation at nonzero separations. At 400 m the correlation from (7) for separations of about 60 km and less are very close to those from (6). Not surprisingly, the analyses from E1 and E4 at each stage of the assimilation cycle were almost identical, until at day 6 there were small observable differences due to vertical exchanges. In contrast, at both 50 and 150 m, the correlations are lower for (7) than for (6) at separations of less than about 65 km and are higher for larger separations. Although these variations are small, they are sufficient to have an impact on the analyses. For example, although the differences at day 2 (Figure 4) were primarily small scale (about 25–50 km), there was a marked difference in horizontal and vertical evolution at day 4. At 50 m, E1 contained a small anticyclone north of a larger coherent cyclone (Figure 4*a*), whereas E4 contained a small scale intense cyclone northwest of a much "flatter" cyclone (Figure 4*b*). The intense cyclone of E4 extended to 150 m with the same intensity, whereas the 150 m analysis of E1 contained much weaker features. For E1 there was some similarity of the 150 m analysis to that at 50 m but not nearly as strong a coherence as for E4. At day 6, there was more

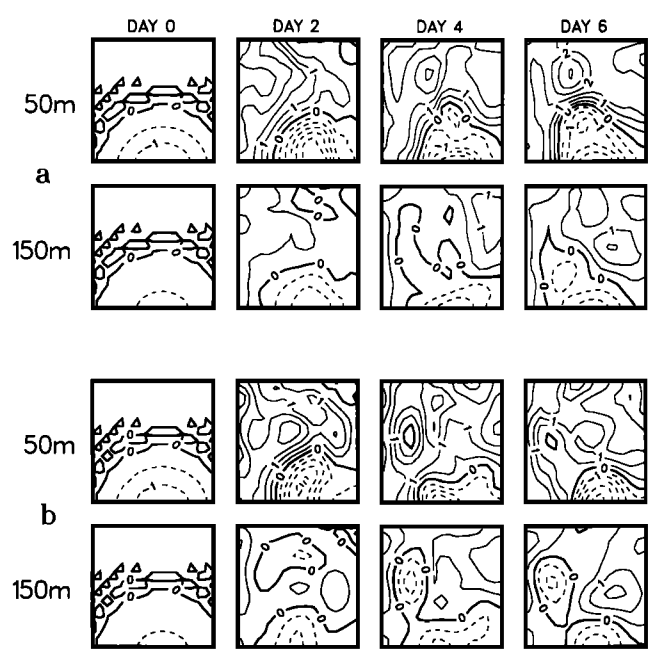

Fig. 4. Stream function at 50 and 150 m during the assimilation cycle for (*a*) E1 and (*b*) E4. Contour interval is 0.5.

TABLE 4. Statistical Comparisons Between Analyses and Between Hindcast Fields for Day 21

	ψ		ζ	
	C	NRMSD	C	NRMSD
		Analyses		
E1 with E2	0.96	0.32	0.77	0.79
E1 with E3	0.96	0.35	0.74	0.84
E1 with E4	0.96	0.28	0.76	0.75
E0 with E5	0.93	0.43	0.84	0.63
		Hindcasts		
E1 with E2	0.93	0.31	0.76	0.67
E1 with E3	0.94	0.31	0.75	0.73
E1 with E4	0.96	0.29	0.84	0.58
E0 with E5	0.99	0.11	0.94	0.31

coherence at these two upper levels for E1 but not nearly as noticeable as for E4.

During the hindcasts (i.e., no additional assimilation beyond the supply of time-dependent boundary information) the QG model allowed the stream function to evolve so as to lessen the differences between the initial fields (i.e., the various analyses), especially with regard to vertical structure (Table 4). This improvement was most noticeable for E0 and E5, where the stream function and potential vorticity differences each dropped by 30%. The other marked agreement was for E1 and E4, where the potential vorticity difference dropped by almost 20%. Some differences remained, often dominated by the boundary forcing. At the end of the hindcast, the remaining difference field at 50 m (E1 − E4) was associated with differences in the flux of potential vorticity by the jet across the eastern boundary into the domain (Figure 5). Initial stream function differences ranged from −2 to 1.5 nondimensional units, with some small-scale variability; the final differences were generally about −0.5 or smaller in magnitude, except for the one dominant feature with amplitude of 2 units. The initial potential vorticity differences ranged from −30 to 60 nondimensional units, again with much small-scale variability; the final differences range from −20 to 40 units with small-scale variations of only about 10 units. At 150 m, differences at the eastern boundary were small and had less of an impact on the integrations; instead, the difference at the end of the hindcast was dominated by an interior feature about 50 km in diameter due to differences in the intensity and penetration of the anticyclone just north of the jet. At the deeper levels, where the flow was much weaker (10% or less of the surface flow), the stream function differences were weak and of domain size directly attributable to differences in the specified boundary values. As was found in other dynamical interpolation experiments in this region [e.g., RMR], over the 15-day integration the dynamical model effectively developed a vertical structure consistent with the dominant variability in the upper levels. This successful model interpolation is probably dependent on the surface-trapped nature of the signal, maintained in the EOF projection to deeper levels independent of the assumed horizontal covariance structure, and the gentle slope of the bathymetry.

The successful hindcast from E5 indicates the strong control of boundary forcing on the evolution of features in this small open ocean domain, at least for these particular realizations: the model evolution of ψ on the largest scales was constrained predominantly by the imposed boundary conditions, accounting for the high correlation in ψ (Table 3). However, the development of the anticyclonic curvature in the E5 hindcast from the cyclone in the initial field demonstrates, in its agreement with the other analyses, the power of dynamical interpolation in evolving the stream function field in the model interior even in this small model domain. This effective forcing of smaller scales by larger scales through nonlinear dynamical coupling was also demonstrated in an open domain atmospheric model by *Errico and Baumhefner* [1987].

The comparison of the analyses for days 36 and 59 and the dynamical hindcasts for day 59 yields similar results, with E1 and E2 outperforming E3 and E4. Only the former are shown in Figure 6 and included in Table 5. The discrepancies between E1 and E2 analyses are more pronounced for day 59 than for any of the previous analysis days: the correlation between stream function fields was only 0.63, compared with about 0.96 for other analyses, and NRMSD was 49%, compared with about 32% for the other analyses. As well as the differences in the structure of the cyclonic region of negative stream function, there are differences in gradient and inflow-outflow locations along the northern boundary. In contrast to the previous set of sensitivity experiments, the better hindcast was obtained using the E2 analyses. An additional hindcast experiment, E6, was run: the QG model was initialized with the E1 field at day 36, and boundary information was supplied by interpolation between that field and the E2 field at day 59. This gave the best hindcast (Table 5), indicating that the sampling strategy of DIII accounted for the difference from the previous sensitivity experiments. In the hindcast experiments of RMR, a bogus positive wind stress curl over the whole domain was necessary for an

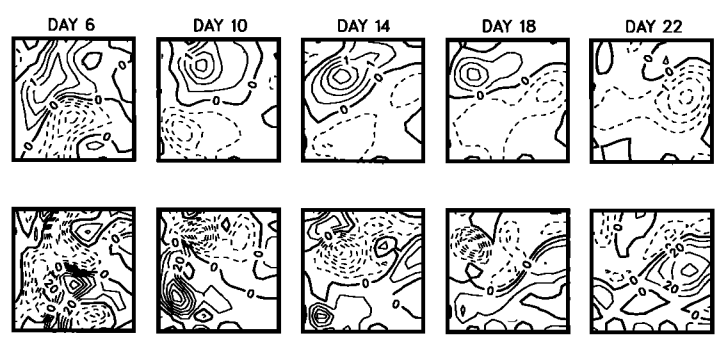

Fig. 5. The differences between hindcasts, E1 − E4: (*a*) stream function (contour interval, 0.5) and (*b*) potential vorticity (contour interval, 10).

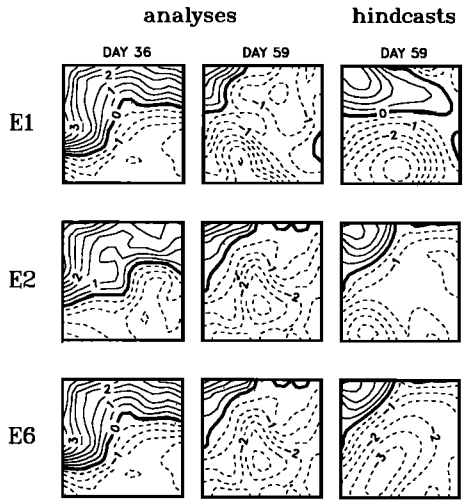

Fig. 6. Analyses of stream function (left) for day 36 and (middle) for day 59, and (right) the dynamical hindcast for day 59. The E6 hindcast used the initial filed from E1 and the final boundary conditions from E2. Contour interval is 0.5.

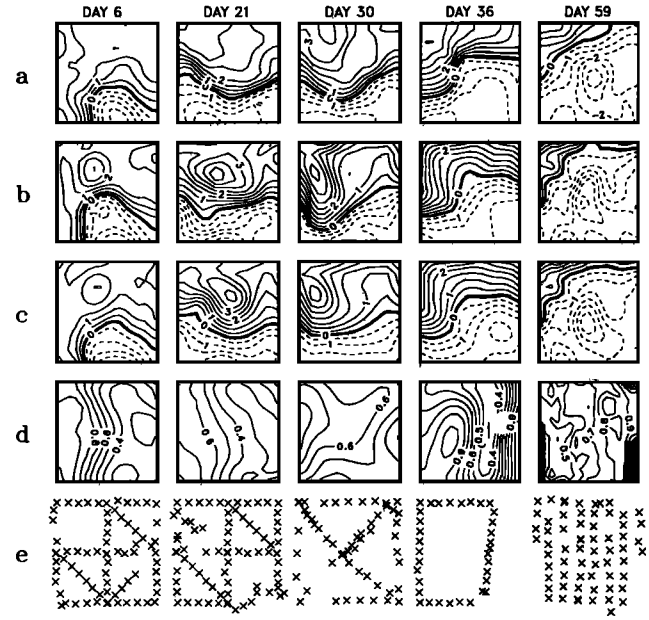

Fig. 7. The analyses for the five OPTOMA11 surveys: (*a*) the statistical objective analyses (E0); (*b*) OI as in E1 but determined during continuous assimilation over 59 days; (*c*) as for Figure 7*b* but with error as determined according to (3) with (4) (contour interval, 0.1); (*d*) 1σ error fields; (*e*) the sampling scheme.

accurate hindcast during this portion of the experiment. Additional experiments [*Rienecker and Mooers*, 1989] found that the imposition of an artificial source of positive vorticity across the northern boundary also improved the hindcast. Here it was found that the necessary vorticity forcing was in the smaller scales across the northern boundary. The rms error over a 23-day hindcast was 31% of the stream function variance for E6, while the error for a 15-day hindcast with artificial curl was 30%; with the artificial vorticity source at the northern boundary the error was 38% [*Rienecker and Mooers*, 1989].

The sampling strategy for DIII differed from the previous surveys in having a more regular coverage of the entire region: north-south tracks were spaced by about 21 km, much less than the 75-km spacing of AI and AII. In addition, the tracks progressed from east to west, i.e., generally downstream.

From the first set of analyses and hindcasts for this small open ocean domain, it is apparent that (1) an analysis technique which reproduced the large-scale (i.e., larger than 50 km) features and used a depth-independent covariance function consistent with the vertical mode representation of the assimilated data produced the best analysis (in the sense of producing a consistent model hindcast), but that (2) in subsequent integrations without further assimilation, the dynamical model effectively "dynamically filtered" the analyses to reduce the impact of their differences, except, primarily, for the influence of differences on the boundary. From the second set of analyses and hindcasts it is apparent that the accuracy of the vorticity estimates at inflow boundary sections is important for successful dynamical interpolation. The observation spacing should be small enough to define the small (about 40 km) scales (yet retain the larger domain-size scales) on the boundary; the appropriate forecast error covariance structure then has shorter scales. If the observation spacing is not sufficient to define these smaller scales, the first set of experiments would indicate that such structure cannot be defined merely by the imposition of shorter covariance scales. This indicates (perhaps not surprisingly) that the chosen global error covariance functions are not accurate (even in this small domain the covariance is likely to be inhomogeneous); however, the accuracy of the hindcasts would also indicate that the chosen functions and scales are not inappropriate.

3.2. *The OPTOMA11 Surveys and Forecast Error Estimates*

In light of the above results, OI analyses for the first four OPTOMA11 surveys (Figure 7) were produced using the covariance function (6) with (a, b) = (80, 100) km. The covariance structure was changed at day 55 of the assimilation to (a, b) = (40, 50) km to produce the final analysis at

TABLE 5. As for Table 3, but for Day 59 Hindcasts

	NRMSD Pointwise Observations	Analyses					
		ψ		$\lvert\nabla\psi\rvert$		ζ	
		C	NRMSD	C	NRMSD	C	NRMSD
E1	0.60	0.76	0.50	0.38	0.89	0.19	0.59
E2	0.45	0.83	0.34	0.58	0.68	0.18	0.58
E6	0.31	0.91	0.37	0.73	0.55	0.29	0.52

day 59. The analyses were produced from a "continuous" model integration; i.e., the analysis for day 21 was produced by integrating from the day 6 analysis with boundary data kept constant until updated by assimilation and so on, to day 59. (In the previous experiments the analysis for day 21 was produced independently from that for day 6, starting from $\psi = 0$ at day 17 instead.) Wind stress curl forcing, as obtained from the data used by RMR, was included. The sampling scheme for each survey is shown in Figure 7*e*. The periods over which data were assimilated to produce the final analysis for each survey are given in Table 1 with the number of data points actually assimilated. The OA fields are shown for comparison (Figure 7*a*). The stream function from the OI using time-dependent error variances in **P**, namely, $\mathbf{P}_k^f$ of (4), is also shown (Figure 7*c*) with the associated 1–standard deviation error fields (Figure 7*d*). For Figure 7*c*, the $D(r)$ of (5) was assumed to grow linearly in time to the climatological variance in 20 days, the estimated decorrelation timescale of the upper ocean in this region [*Rienecker et al.*, 1988], after which it was held constant in time. The real model error growth is likely to be slower, but its determination requires comparison with observations. An estimate could be made using a Kalman filter as was done by *Cohn* [1982]; however, the time scale was chosen from the observations for consistency with the spatial scales (it roughly represents the Rossby wave-like time-scale associated with a spatial scale the same as the stream function decorrelation scale, compared with the advective time scale in the jet which is only about 2 days at 50 m). The OI with constant error variances will be referred to as OI1, and that with time-dependent variances, as OI2.

Qualitatively, the two sets of OI analyses are similar; however, the fields produced using OI2 are smoother than those produced with OI1. This is to be expected, since OI2 gives more weight to the forecast stream function in areas recently influenced by assimilation than does OI1 and so the data assimilation is less likely to introduce artificial, sharp gradients or sharply curved features. The temporal evolution across these snapshots is more coherent than that of the OA fields, in which no account can be made for the appearance of the anticyclone of day 21 or the sharpened gradient in the center of the domain at day 36.

The two OI analyses for day 6 are similar in the existence and location of the small-scale (diameter of about 40 km) anticyclone, but the gradients in the OI2 analysis (Figure 7*c*) compare better with those of the OA. In the regions most recently updated (as indicated by the low error contours), however, the two OI analyses are in good agreement. The anticyclone in the northern part of the domain at day 21, having developed from the small anticyclone at day 6, was more intense and penetrated farther into the domain in the OI analyses than in the OA or the E1 analyses formed by assimilation from $\psi = 0$ at day 17 (Figure 3). The time series from 150 and 400 m (not shown) indicate that this anticyclone was formed by the vertical locking of separate anticyclonic features at these three depths: the one at 50 m propagated slightly eastward and those at the lower two levels (see the anticyclone in the east at 150 m in Figure 4*a*) propagated westward to interlock vertically and intensify. The curvature of the jet at day 21 in the center of the OI2 analysis is in better agreement with that from OA than from OI1 analysis, although the stronger gradient of the latter agrees better with the OA. The error is low over most of the domain because of the short transit time for this survey.

At day 30 the anticyclone in both OI analyses remained narrower than in the OA and penetrated farther into the domain. It evolved slightly from its form and location at day 21 and appears to be a robust feature, as its location was sampled twice during survey 3. The streamline curvature in the northeastern quadrant in the OI was cyclonic, in contrast with the OA, and showed some of the influence of positive wind stress curl forcing during this period [RMR]. The gradient and jet orientation in the western part of the OI2 analysis agreed better with the OA than the OI1 analysis. The sharper gradient and stronger curvature from OI1 is a result of stronger gradients introduced by the OI when it does not place greater confidence in the forecast stream function.

The OI analyses at day 36 were more in keeping with the synoptic fields from aircraft data taken 6 days later (not used in these analyses because the profiles were very shallow) than was the OA field (see day 200 in Figure 11 of RMR, equivalent to day 42 here). The NRMSD between the vertical shear (ψ(50 m) − ψ(150 m)) at day 42 of the continuous assimilation integrations and that from the aircraft data was 55%. This appears high, but the shear variance used for normalization was only 0.95, whereas the normalization factor for stream function differences was 2.03. In comparison, the vertical shear difference in the appropriate 13-day hindcast experiment of RMR using OA fields (where the boundary information supplied by the aircraft data should have improved the comparison) was 79%.

At day 59, the fields from the OA and OI2 are in better agreement with respect to the width of the jet compared with the fields from OI1, although the two OI analyses give a higher estimate of the gradient in the extreme northwest of the domain. Both OI analyses show the cyclone about 20 km southwest of its location in the OA, but with similar intensity. On the whole, it seems that the use of (4) and (5) with updated variances bounded by climatology may give a more accurate representation of the fields than the constant variance OI.

4. SUMMARY

In this paper, optimal interpolation (OI) has been used to assimilate hydrographic observations into a QG model of a 150-km-square open domain off northern California. Since the model error covariances are unknown a priori, experiments were conducted to investigate the sensitivity of analyses produced independently for four surveys to the parameters used in an assumed model error covariance function. Since there were no independent observations with which to assess the quality of the analyses, a comparison was made through dynamical hindcasts. The QG model was initialized with the OI analysis for the first survey and the model "forecast" the interior of the second survey using boundary values based on analyses of both surveys. In this use of hindcasts to assess the analyses, the dynamical model essentially (re)defines "truth": the time and space scales of interest, and the only ones that can be verified, are those consistent with QG dynamics and the resolution of the model. A posteriori comparisons of the hindcasts with point measurements show good agreement (Tables 3 and 5).

For the surveys with an irregular and rather coarse sampling strategy, the smoother analysis fields produced with error covariance scales identical to those of the observed stream function yielded better hindcast results than the analyses produced with reduced covariance scales. Based on differences during the model integrations for the first part of the observing period, the hindcasts were heavily influenced by vorticity estimates across the inflow on the eastern boundary. For the second half of the observing period, the hindcasts were heavily influenced by the flux of vorticity on small scales across the northern boundary. These small scales (which were resolved by the finer, more regular sampling strategy of the final OPTOMA11 survey) and the locations of inflow across the boundary were best defined by shorter error covariance scales.

Differences in the analyses near inflow boundary points on scales of 20–50 km led to 50-km scale differences in the model interior at the upper model levels after a 15-day integration. Initial differences in the domain interior on these scales and smaller tended to decay in time owing to the strong control of the boundary forcing for this size domain and the effective dynamical filtering afforded by the model. Differences at the lower model levels were weak, of domain scale, and totally attributable to stream function differences on the boundary. Similar remarks would apply to the results of *De Mey and Robinson* [1987], who performed open boundary computations in a similar size domain relative to the internal radius for the Polymode region of the northwest Atlantic. This size domain is typical for mesoscale ocean sampling schemes (see also *Hua* [1988] for the Tourbillon site in the eastern North Atlantic). The results here are consistent with those of *Errico and Baumhefner* [1987], who performed a predictability study for an atmospheric limited-area (open boundary) mesoscale model for the continental United States; the limited-area model domain was also comparable in size, for atmospheric scales, to the domain used here for the ocean.

In the case of numerical weather prediction, where data over the entire model domain are collected (and assimilated) essentially simultaneously, analysis errors have the same spatial scale as the observation separation [*Lorenc*, 1988]. In our case the error structure is complicated by the space-time sampling problem: in regions of strong advection, the errors can propagate through the domain very quickly, resulting in larger error scales. This study (and that of *Errico and Baumhefner* [1987] for the atmosphere) shows that for an open domain once the large scales are defined (essentially by the boundary values) the errors on small scales diminish due to diffusion until the errors become concentrated near synoptic/mesoscale features because of intensity and/or phase errors (see Figure 5). In the case of perfect boundary data, much of the mesoscale error may be advected out of the domain; in our case, imperfect boundary data contribute to the interior mesoscale error. For most of the OPTOMA11 survey, the best analysis (in a QG-consistent sense) was obtained using a forecast error covariance scale the same as that of the observed mesoscale stream function. This scale is somewhat justified a posteriori by the scale of differences between hindcasts based on different (but similar) analyses and by the scales defined only by the boundary data (experiment E5 above). It also happens to be about the same as defined by the observation separation (the larger of the along-track and cross-track data spacing). For the final survey, the best analysis was obtained with reduced error covariance scales because of the finer observation resolution and the importance of small-scale vorticity forcing at the northern boundary. However, if the observation spacing is not sufficient to define the smaller scales, this study indicates that such structure cannot be defined merely by the imposition of shorter error covariance scales.

In the continuous assimilation over the entire OPTOMA 11 observing period, covering 59 days in all, analyses for the first four surveys were produced using the functional form of the observed stream function covariance for the forecast stream function error covariance. Reduced covariance scales were used for the final survey. A modified form of OI in which the forecast error variances were updated according to the analysis error variance and an assumed model error growth rate was also used. This allowed the OI to identify regions already influenced by assimilation and so to place more confidence in the forecast stream function there. The analyses from the updated variances were spatially smoother and often in better agreement with the observations than the OI analyses from constant variances. The two sets of OI analyses were temporally smoother than the fields from statistical objective analysis (OA) and in better agreement with the only independent data available for comparison (synoptic aircraft data acquired 6 days after the relevant OI analysis). The marked differences between the OA and OI analyses lay in the existence or location and intensity of smaller mesoscale features and associated gradients. Whereas the evolution inferred from the OA fields from day 6 to 21 required the influence of external boundary forcing to produce the anticyclone north of the jet, the evolution from the OI analyses showed the interior evolution (the vertical locking of anticyclonic features in the upper levels of the model) to be important as well.

This study has demonstrated the efficacy of using OI with real observations to produce synoptic estimates of mid-latitude mesoscale variability. The apparent improvement in the analyses afforded by the updated variance form of OI indicates that the use of the Kalman filter, which would also account for advection of variance information, would probably improve the analysis further. In any case, the interplay between the dynamical model and data through the assimilation cycle, wherein data are synoptically ingested to correct the model fields and then the model dynamically filters the resulting analyses, decreases the impact of errors associated with incorrect assumptions for the model forecast error covariance. In this way, data assimilation provides a powerful tool for presenting and interpreting asynoptic data.

Clearly, there are many issues not addressed here. Perhaps the most important is consideration of the influence of the inhomogeneity of the error covariance: it is likely that the covariance structure near the boundaries is different from that in the interior of the model domain. As is shown here, the vorticity estimates at the inflow boundary points can have a marked impact on the evolution of the stream function fields, so it is important to have good estimates of the error covariance near the boundary. It is also important for the sampling strategy to define the vorticity scales on the boundary adequately. The issues of parameter sensitivity should be addressed in a much larger domain so that there is less influence of the boundary data on the internal evolution of the fields. In addition, the distinction between the resolution or nonresolution of eddy scales in both the data and the

model should be addressed. The effect of different sampling strategies should be considered further. Unfortunately, the limiting factor in the validation of different methodologies remains the paucity of real observations.

Acknowledgments. Support for this study was provided through NASA RTOP 971-161-20-31 (M.M.R.) and ONR contract N00014-90-J-1125 (R.N.M.) and is gratefully acknowledged. The OPTOMA program was a joint program between the Naval Postgraduate School (principal investigator, Chris Mooers) and Harvard University (principal investigator, Allan Robinson), sponsored by the Office of Naval Research.

REFERENCES

Adamec, D., Predictability of quasigeostrophic flows, *J. Phys. Oceanogr.*, *19*, 1753–1764, 1989.

Bengtsson, L., M. Ghil, and E. Kallen (Eds.), *Dynamic Meteorology: Data Assimilation Methods*, 330 pp., Springer-Verlag, New York, 1981.

Bennett, A. F., Inverse methods for assessing ship-of-opportunity networks and estimating winds from tropical expendable bathythermograph data, *J. Geophys. Res.*, *95*, 16,111–16,148, 1990.

Bennett, A. F., and W. P. Budgell, The Kalman smoother for a linear quasi-geostrophic model of ocean circulation, *Dyn. Atmos. Oceans*, *13*, 219–267, 1989.

Bennett, A. F., and P. C. McIntosh, Open ocean modelling as an inverse problem: Tidal theory, *J. Phys. Oceanogr.*, *12*, 1004–1018, 1982.

Charney, J. G., R. Fjortoft, and J. Von Neumann, Numerical integration of the barotropic vorticity equation, *Tellus*, *2*, 237–254, 1950.

Cohn, S. E., Methods of sequential estimation for determining initial data in numerical weather prediction, *Rep. CI-6-82*, Courant Inst. of Math. Sci., 183 pp., 1982.

Cohn, S. E., and L. L. Morone, The effect of horizontal gradients of height-field forecast error variances upon OI forecast error statistics, *Office Note 296*, 37 pp., NOAA Natl. Meteorol. Cent., Washington, D. C., 1984.

De Mey, P., and Y. Menard, Synoptic analysis and dynamic adjustment of GEOS 3 and Seasat altimeter eddy fields in the northwest Atlantic, *J. Geophys. Res.*, *94*, 6221–6231, 1989.

De Mey, P., and A. R. Robinson, Assimilation of altimeter eddy fields in a limited-area quasigeostrophic model, *J. Phys. Oceanogr.*, *17*, 2280–2293, 1987.

Errico, R., and D. Baumhefner, Predictability experiments using a high-resolution limited-area model, *Mon. Weather Rev.*, *115*, 488–504, 1987.

Gaspar, P., and C. Wunsch, Estimates from altimeter data of barotropic Rossby waves in the northwestern Atlantic, *J. Phys. Oceanogr.*, *19*, 1821–1844, 1989.

Harlan, J., Jr., and J. J. O'Brien, Assimilation of scatterometer winds into surface pressure fields using a variational method, *J. Geophys. Res.*, *91*, 7816–7836, 1986.

Hua, B. L., The internal barotropic instability of surface-intensified eddies, II, Modeling of the Tourbillon site, *J. Phys. Oceanogr.*, *18*, 56–71, 1988.

Long, R. B., and W. C. Thacker, Data assimilation into a numerical equatorial ocean model, II, Assimilation experiments, *Dyn. Atmos. Oceans*, *13*, 413–439, 1989.

Lorenc, A. C., Analysis methods for numerical weather prediction, *Q. J. R. Meteorol. Soc.*, *112*, 1177–1194, 1986.

Lorenc, A. C., A practical approximation to optimal four-dimensional objective analysis, *Mon. Weather Rev.*, *116*, 730–745, 1988.

McPherson, R. D., K. H. Bergman, R. E. Kistler, G. E. Rasch, and D. S. Gordon, The NMC operational global data assimilation system, *Mon. Weather Rev.*, *107*, 1445–1461, 1979.

Miller, R. N., Toward the application of the Kalman filter to regional open ocean modeling, *J. Phys. Oceanogr.*, *16*, 72–86, 1986.

Miller, R. N., and A. F. Bennett, Numerical simulation of flows with locally characteristic boundaries, *Tellus Ser. A*, *40*, 303–323, 1988.

Miller, R. N., and M. A. Cane, A Kalman filter analysis of sea level height in the tropical Pacific, *J. Phys. Oceanogr.*, *19*, 773–790, 1989.

Miller, R. N., A. R. Robinson, and D. B. Haidvogel, A baroclinic quasi-geostrophic open ocean model, *J. Comput. Phys.*, *50*, 38–70, 1983.

Rienecker, M. M., and C. N. K. Mooers, A summary of the OPTOMA program's mesoscale ocean prediction studies in the California Current system, in *Mesoscale/Synoptic Coherent Structures in Geophysical Turbulence*, edited by J. C. J. Nihoul and B. M. Jamart, pp. 519–548, Elsevier, New York, 1989.

Rienecker, M. M., C. N. K. Mooers, and A. R. Robinson, Dynamical interpolation and forecast of the evolution of mesoscale features off northern California, *J. Phys. Oceanogr.*, *17*, 1189–1213, 1987.

Rienecker, M. M., C. N. K. Mooers, and R. L. Smith, Mesoscale variability in current meter measurements in the California Current system off northern California, *J. Geophys. Res.*, *93*, 6711–6734, 1988.

Robinson, A. R., J. A. Carton, N. Pinardi, and C. N. K. Mooers, Dynamical forecasting and dynamical interpolation: An experiment in the California Current, *J. Phys. Oceanogr.*, *16*, 1561–1579, 1986.

Thacker, W. C., Fitting models to inadequate data by enforcing spatial and temporal smoothness, *J. Geophys. Res.*, *93*, 10,655–10,665, 1988.

White, W. B., C.-K. Tai, and W. R. Holland, Continuous assimilation of Geosat altimetric sea level observations into a numerical synoptic ocean model of the California Current, *J. Geophys. Res.*, *95*, 3127–3148, 1990*a*.

White, W. B., C.-K. Tai, and W. R. Holland, Continuous assimilation of simulated Geosat altimetric sea level into an eddy-resolving numerical ocean model, 1, Sea level differences, *J. Geophys. Res.*, *95*, 3219–3234, 1990*b*.

M. M. Rienecker, Oceans and Ice Branch, NASA Goddard Space Flight Center, Greenbelt, MD 20771.

R. N. Miller, College of Oceanography, Oregon State University, Corvallis, OR 97331.

(Received June 7, 1990;
Revised May 24, 1991;
Accepted May 28, 1991.)